Icarus 219 (2012) 676–688

Contents lists available at SciVerse ScienceDirect

Icarus

journal homepage: www.elsevier.com/locate/icarus

Physical properties of trans-neptunian binaries (120347) Salacia–Actaea and (42355) Typhon–Echidna

J.A. Stansberry [a,*], W.M. Grundy [b], M. Mueller [c], S.D. Benecchi [d], G.H. Rieke [a], K.S. Noll [f], M.W. Buie [e], H.F. Levison [e], S.B. Porter [b], H.G. Roe [b]

[a] Steward Observatory, 933 N. Cherry Ave., University of Arizona, Tucson, AZ 85721, USA
[b] Lowell Observatory, Flagstaff, AZ 86001, USA
[c] SRON LEA, Netherlands Institute for Space Research, Postbus 800, Groningen 9700AV, The Netherlands
[d] Planetary Science Institute, Tucson, AZ 85719, USA
[e] Southwest Research Institute, Boulder, CO 80302, USA
[f] Space Telescope Science Institute, Baltimore, MD 21218, USA

ARTICLE INFO

Article history:
Received 4 November 2010
Revised 23 March 2012
Accepted 27 March 2012
Available online 5 April 2012

Keywords:
Kuiper belt
Trans-neptunian objects
Centaurs

ABSTRACT

We report new *Hubble Space Telescope* and *Spitzer Space Telescope* results concerning the physical properties of the trans-neptunian object (TNO) binaries (120347) Salacia–Actaea (formerly 2004 SB_{60}), and (42355) Typhon–Echidna (formerly 2002 CR_{46}). The mass of the (120347) Salacia–Actaea system is $4.66 \pm 0.22 \times 10^{20}$ kg. The semi-major axis, period, and eccentricity of the binary orbit are $a = 5619 \pm 87$ km, $P = 5.49380 \pm 0.00016$ days, and $e = 0.0084 \pm 0.0076$, respectively. In terms of the ratio of the semimajor axis to the radius of the Hill sphere, a/r_H, (120347) Salacia–Actaea is the tightest TNO binary system with a known orbit. Based on hybrid Standard Thermal Model (hybrid-STM) fits to the data, the effective diameter and V-band geometric albedo of the system are $D = 954 \pm 109$ km (making it one of the largest known TNOs), and $p_V = 3.57^{+1.03}_{-0.72}\%$. Thermophysical models for (120347) Salacia suggest that it probably has a thermal inertia $\leqslant 5$ J m^{-2} s$^{-1/2}$ K^{-1}, although we cannot rule out values as high as 30 J m^{-2} s$^{-1/2}$ K^{-1}. Based on the magnitude difference between Salacia and Actaea, $\delta = 2.37 \pm 0.06$, we estimate their individual diameters to be $d_1 = 905 \pm 103$ km and $d_2 = 303 \pm 35$ km. The mass density of the components is $\rho = 1.16^{+0.59}_{-0.36}$ g/cm^3. Hybrid-STM fits to new *Spitzer* data for Typhon–Echidna give an effective diameter and V-band geometric albedo for the system of $D = 157 \pm 34$ km, and $p_V = 6.00^{+4.10}_{-2.08}\%$. Thermophysical models for (42355) Typhon suggest somewhat lower albedos (probably no higher than about 8.2%, as compared to the hybrid-STM upper limit of 10.1%). Taken together with the previously reported mass, this diameter indicates a density of $\rho = 0.60^{+0.72}_{-0.29}$ g/cm^3, consistent with the very low densities of most other TNOs smaller than 500 km diameter. Both objects must have significant amounts of void space in their interiors, particularly if they contain silicates as well as water–ice (as is expected). The ensemble of binary-TNO densities suggests a trend of increasing density with size, with objects smaller than 400 km diameter all having densities less than 1 g/cm^3, and those with diameters greater than 800 km all having densities greater than 1 g/cm^3. If the eccentricity of the binary orbit of (42355) Typhon–Echidna is not due to recent perturbations, considerations of tidal evolution suggest that (42355) Typhon–Echidna must have a rigidity close to that of solid water ice, otherwise the orbital eccentricity of the system would have been damped by now.

1. Introduction

There are about 70 known binary trans-neptunian objects (TNOs) and Centaurs, with about 50% of them belonging to the "cold classical" dynamical class (*e.g.* Noll et al., 2008). Binaries are of distinct interest because of the insights they provide into the dynamics and environment in which they formed, and because their masses (and mass densities) can be determined via remote observation. Noll et al. (2008) summarized the physical properties of 13 TNO binary systems. Eight TNO binaries have published mass densities: (47171) 1999 TC_{36} (Stansberry et al., 2006; Benecchi et al., 2010), (136108) Haumea (Rabinowitz et al., 2006; Lellouch et al., 2010), (26308) 1998 SM_{165} (Spencer et al., 2006), (136199) Eris (Brown and Schaller, 2007), (65486) Ceto (Grundy et al., 2007; Santos-Sanz et al., 2012), (42355) Typhon (Grundy et al., 2008), (90482) Orcus (Brown et al., 2010), and (50000) Quaoar (Fraser and Brown, 2010). In most cases the system masses are

* Corresponding author. Fax: +1 520 621 9555.
E-mail address: stansber@as.arizona.edu (J.A. Stansberry).

0019-1035/$ - see front matter © 2012 Elsevier Inc. All rights reserved.
http://dx.doi.org/10.1016/j.icarus.2012.03.029

determined from *Hubble* (HST) observations that resolve the binary components, although adaptive optics on the largest ground-based telescopes also contributes. The size of the binaries are usually derived from *Spitzer Space Telescope* thermal observations. Because the components are not resolved by *Spitzer* only the effective diameter and albedo of the system (*i.e.* the diameter and albedo of an object with the same projected area as the two binary components combined) can be determined.

Here we report the results from a *Hubble* visible-light imaging study (augmented by two near-IR observations at Keck), and a *Spitzer* thermal-radiometry study of the binary TNOs (120347) Salacia–Actaea and (42355) Typhon–Echidna. The short-wavelength data constrain the relative sizes of the binary components (through the difference in their magnitudes), their absolute visual magnitudes and colors, the geometry of the binary orbit, and the mass of the system. The *Spitzer* data constrain the effective diameter and albedo of the systems, and give some idea of the temperature distribution on their surfaces. In the case of (120347) Salacia we are able to place meaningful constraints on the thermal inertia of the surface materials. Taken together, the *Hubble* and *Spitzer* data sets allow a determination of the mass density of the systems. The results for (120347) Salacia–Actaea (which we generally refer to as Salacia hereafter) are entirely new; those for (42355) Typhon–Echidna (which we generally refer to as Typhon hereafter) update the results presented in Grundy et al. (2008).

1.1. (120347) 2004 SB_{60}

Salacia was discovered in images taken in September, 2004, at Palomar by Roe et al. (2005). Two years later Noll et al. (2006a) reported discovery of a binary companion to Salacia in *Hubble* ACS images acquired in September, 2006. The heliocentric orbit of Salacia is non-resonant, with modest eccentricity, but a large inclination (Minor Planet Center (MPC) orbital elements of $a = 42.3$ AU, $e = 0.11$, $i = 23.9°$). It is classified as a scattered-extended object in the Deep Ecliptic Survey (DES) classification (Elliot et al., 2005), and is a classical KBO in the classification of Gladman et al. (2008). Whether it is a member of the hot classical disk or of the scattered extended disk may be a non-distinction if those populations are part of a single population that formed as a result of the outward migration of Neptune (Gomes, 2003, 2011). Salacia lies within the region of orbital-element space associated with the Haumea collisional family (Brown et al., 2007), but lacks the strong water–ice near-IR absorption features that have become a de facto test of membership in the family (Schaller and Brown, 2008). (Note that the family members with strong water–ice absorptions also exhibit a slightly blue optical color; it has been suggested that the family includes additional members based on optical color alone (Ragozzine and Brown, 2007; Snodgrass et al., 2010)).

Visible photometry for the components of Salacia was recently published by Benecchi et al. (2009), based on *Hubble* WFPC2 data. They transform the *Hubble* results to the Johnson/Cousins filter system, deriving $(V–I)$ colors of 0.87 ± 0.01 and 0.89 ± 0.02 for the primary and secondary, respectively. Thus the Salacia system is moderately red (Solar $(V–I) = 0.69$; *e.g.* Doressoundiram et al., 2008). Thirouin et al. (2010) find a very low-amplitude rotational lightcurve for Salacia (3% amplitude), with a single-peaked rotational period of 6 h, or a double-peaked period of 12 h (Sheppard et al. (2008) suggest that for an object with such a weak lightcurve and large size, the single-peaked interpretation is likely to be correct). Here we present significantly improved values for the absolute V band magnitudes of the system and the components (previously given in Benecchi et al., 2009), the solution for the binary orbit (including system mass), and the results from our *Spitzer* observations (albedo and effective system diameter).

1.2. (42355) Typhon–Echidna

(42355) Typhon, provisional designation 2002 CR_{46}, was the first binary Centaur discovered (Noll et al., 2006b); the secondary is named Echidna. Typhon's heliocentric orbital elements (MPC) are $a = 37.6$ AU, $e = 0.53$, and $i = 2.43°$. Again the DES (Elliot et al., 2005) and Gladman et al. (2008) dynamical classifications differ, with the DES classifying Typhon as a Centaur with an expected dynamical lifetime <10 Myr, while Gladman et al. group it with the scattered-disk objects. The difference between these classes is primarily just whether the aphelion is outside Neptune's orbit: dynamically the two groups form a continuum. With a $(V–R)$ color of about 0.5 (Tegler et al., 2003; Rabinowitz et al., 2007; DeMeo et al., 2009), Typhon is also moderately red (Solar $(V–R) = 0.36$ (Cousins system); *e.g.* Doressoundiram et al., 2008). Early lightcurve observations of Typhon were inconclusive, limiting the amplitude of any variations to $\leqslant$15% (Ortiz et al., 2003; Dotto et al., 2008). New observations (Thirouin et al., 2010) indicate a weak lightcurve (amplitude $\simeq$7%), and a single-peaked rotation period for the body of 9.7 h (for such a small object, the lightcurve might result from its shape, in which case the rotation period would be 19.4 h). The orbital period for the system is 18.97 days (Grundy et al., 2008), so such a rotation period would imply that the Typhon–Echidna system is not tidally locked. Stansberry et al. (2008) found an effective diameter for the Typhon–Echidna system of 175 ± 19 km, based on a *Spitzer* detection of the system at 70 μm. Below we present results based on new *Spitzer* thermal observations, and re-examine the conclusions of Grundy et al. (2008) for the size, albedo and density of this system. More recently, Typhon was observed at wavelengths of 70, 100 and 160 μm using the *Herschel Space Telescope* (Müller et al., 2010), resulting in an effective diameter for the system of 144 ± 10 km.

2. Astrometry, visible photometry

The Salacia system was observed by *Hubble* in two separate programs. The first was Noll et al. Cycle 14 program 10514, which surveyed 68 TNOs searching for binaries. This program obtained 4 clear-filter images of the system using the High Resolution Camera (HRC) of the Advanced Camera for Surveys (ACS; Ford et al., 1996), leading to the initial discovery of the satellite (Noll et al., 2006a). Additional follow-up observations were obtained through Grundy et al. Cycle 16 program 11178, using the Planetary Camera (PC) of the Wide Field and Planetary Camera 2 (WFPC2; McMaster et al., 2008) mostly with the F606W filter (a broad-band filter with central wavelength 606 nm). We obtained a final observation of the system using the NIRC2 instrument with laser guide star adaptive optics (Le Mignant et al., 2006) at the W.M. Keck telescope, in the H band. Example images are shown in Fig. 1. Geometric circumstances along with astrometric and photometric measurements are listed in Table 1. Images were analyzed by fitting Tiny Tim model PSFs (Krist and Hook, 2004) to each image frame, with observing methods and astrometric reduction details described in Grundy et al. (2009, 2011). JAS and photometric reduction details described in Benecchi et al. (2009). We report visit averages, with the scatter between observations in each visit used to estimate 1σ measurement uncertainties.

The weighted mean magnitude difference between primary and secondary is $\Delta\text{mag} = 2.372 \pm 0.060$ mags, implying a diameter ratio ($d_1/d_2 = 10^{\Delta\text{mag}/5}$) of 2.98 if the components share the same albedo. Table 2 summarizes the photometric results, converted to absolute magnitudes in V band, for both Salacia and (42355) Typhon–Echidna. The differences from the Benecchi et al. (2009) values result from our inclusion of 6 single-color visits (they used only one multi-color visit for Salacia, and we have combined the (42355)

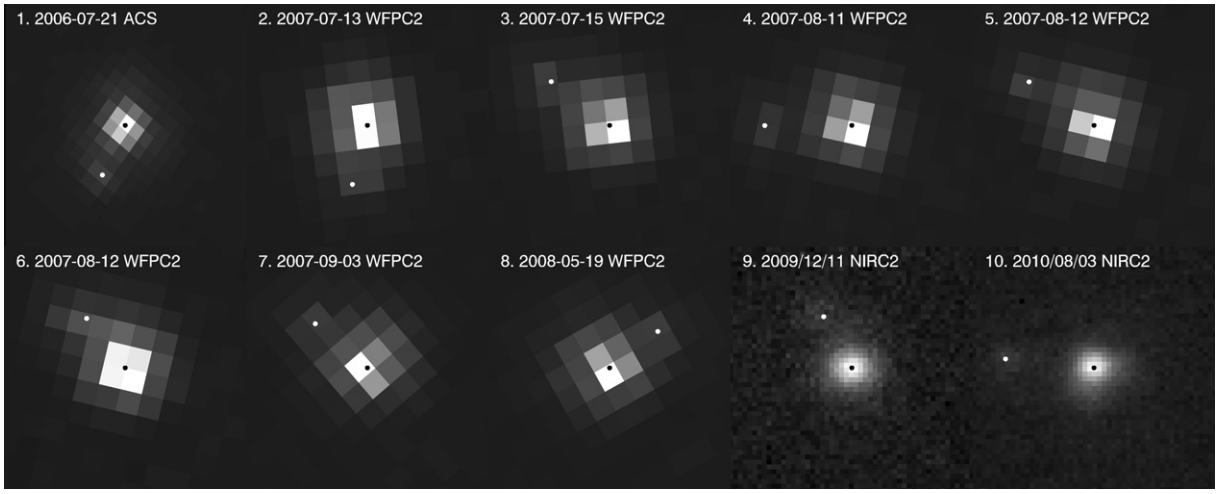

Fig. 1. A single frame from each of the 8 *Hubble* visits and the two NIRC2/Keck observation of (120347) Salacia–Actaea. Each frame has been stretched linearly from minimum to maximum signal, projected to sky-plane geometry with North up and East to the left, centered on the primary, and zoomed into show a 0.5 × 0.5 arcsec region. Note the smaller, more distorted ACS pixels in the first visit, which do a better job of sampling the PSF. Fitted positions of the primary and secondary are indicated by black and white dots, respectively. The pixel scales (in ″/pixel) for the three instruments are ≃0.027 (ACS/HRC: varies across the instrument FOV and pixels are not square), 0.0455 (WFPC2/PC), and 0.009963 (NIRC2).

Table 1
Astrometric observations of (120347) Salacia–Actaea.

Observation date[a]	Inst.[b]	r[c] (AU)	Δ[c] (AU)	α[c] (°)	δx[d] (″)	δy[d] (″)	$V_{primary}$[e] (mag)	$V_{secondary}$[e] (mag)
06/07/21 21.9583[h]	A	43.791	43.165	1.06	−0.04706(70)	+0.10224(50)	–	–
07/07/13 21.1017[h]	W	43.882	43.377	1.16	+0.0219(39)	−0.111(13)	21.037(45)	23.80(16)
07/07/15 19.9142[h]	W	43.882	43.352	1.14	+0.1237(45)	+0.0921(21)	21.005(11)	23.125(45)
07/08/11 11.1392[h]	W	43.889	43.079	0.80	−0.1778(15)	−0.0036(30)	20.964(10)	23.371(27)
07/08/12 6.6864[h]	W	43.889	43.073	0.79	+0.1279(39)	+0.0940(19)	20.968(03)	23.194(21)
07/08/12 9.8156[h]	W	43.889	43.072	0.79	+0.1008(86)	+0.0989(32)	20.984(03)	23.126(19)
07/09/03 9.7183[h]	W	43.895	42.972	0.54	+0.1031(36)	+0.0995(35)	20.943(10)	23.189(28)
08/05/19 18.5686[h]	W	43.960	44.290	1.24	−0.1010(13)	+0.0742(10)	21.180(07)	23.408(29)
09/12/11 6.5120[h]	N	44.100	44.082	1.28	+0.0580(61)	+0.1056(30)	–	–
10/08/03 9.7339[h]	N	44.157	43.457	0.97	+0.1827(30)	+0.0184(30)	–	–

[a] Dates are average UT mid-times of observations at the location of the observer (HST or Keck). Date is in YY/MM/DD format.
[b] Instrumentation used. A: *Hubble* ACS/HRC; W: *Hubble* WFPC2/PC; N: Keck NIRC2.
[c] The distance from the Sun to the target is r and from the observer to the target is Δ, and α is the phase angle.
[d] Relative right ascension δx and relative declination δy are computed as $\Delta x = (\alpha_2 - \alpha_1)\cos(\delta_1)$ and $\Delta y = \delta_2 - \delta_1$, where α is right ascension, δ is declination, and subscripts 1 and 2 refer to primary and secondary, respectively. 1σ uncertainties in the final 2 digits are indicated in parentheses. These are estimated from the scatter among each set of dithered images with floors of 1 and 0.5 mas for WFPC2 and ACS/HRC observations, respectively, as described in the text.
[e] Mean V-band photometry of primary and secondary bodies during each visit was derived from WFPC2/PC F606W images as described by Benecchi et al. (2009). The first visit was a clear filter observation from which V-band photometry cannot be reliably derived. The 2009 and 2010 data was taken in the H-band, and no photometric standards were observed. 1σ uncertainties of the mean in the final 2 digits are indicated in parentheses.

Typhon data given there with additional ground-based measurements). The equal-albedo assumption is supported by the observation that the components of Salacia (and nearly all TNO binaries) have the same visible color ($(V–I)$ = 0.87 and 0.89 for the primary and secondary, respectively: Benecchi et al., 2009). Our use of G = 0.15 is appropriate for low-albedo objects (*e.g.* Brucker et al., 2009), and consistent with the phase behavior of low-albedo TNOs (*e.g.* Rabinowitz et al., 2007; Sheppard, 2007). Because of the small phase angles involved, uncertainties in the actual phase behavior of our targets lead to uncertainties in the phase corrections of perhaps 2 percent.

2.1. Binary parameters for Salacia–Actaea

The astrometric measurements of the Salacia system were used to constrain Keplerian orbit solutions, using techniques described previously (Grundy et al. 2008, 2009, 2010). Since the observations span a relatively short period of time, the parallax is insufficient to distinguish between an orbit solution and its mirror image through the sky plane at the time of the observations; consequently we report two orbit solutions (Table 3). Because the two solutions have nearly the same χ^2 value, we adopt the following values for the binary parameters, with error bars inflated to encompass the uncertainties associated with both solutions. These values are period P = 5.49380 ± 0.00016 days, semimajor axis a = 5619 ± 89 km, and eccentricity e = 0.0084 ± 0.0076, leading to a system mass of M_{sys} = 4.38 ± 0.16 × 10^{20} kg. The orbit of the system projected onto the sky, along with the relative astrometry and uncertainties, are shown in Fig. 2. In terms of the ratio of the semimajor axis to the radius of the Hill sphere, a/r_H = 0.0023, (120347) Salacia–Actaea is the tightest TNO binary system with a known orbit.

3. *Spitzer* space telescope observations and data analysis

We observed Salacia and Typhon with the Multiband Imaging Photometer for *Spitzer* (MIPS, Rieke et al., 2004) in its 24 and 70 μm bands. The data for Salacia were collected under observing program 30081 (PI J. Stansberry); those for Typhon were taken under program 40016 (PI G. Rieke). (Earlier *Spitzer* 70 μm-only results

Table 2
Adopted visible photometry.

Quantity	Magnitude[a]
Salacia–Actaea	
H_V primary[b]	4.476 ± 0.013
H_V secondary[b]	6.850 ± 0.053
H_V system[b]	4.360 ± 0.011
Δ^b_{mag}	2.372 ± 0.060
Typhon–Echidna	
H_V primary[c]	8.035 ± 0.040
H_V secondary[c]	9.276 ± 0.064
H_V system[c]	7.715 ± 0.035
Δ^c_{mag}	1.241 ± 0.069

[a] Absolute magnitudes are computed assuming G = 0.15 in the H and G photometric system (Bowell et al., 1989).
[b] Salacia–Actaea values are derived from the HST photometry in Table 1.
[c] Photometry of the components of Typhon-Echidna are from Grundy et al. (2008). Those are converted to total magnitudes for the system and then combined with additional photometry from Tegler et al. (2003) and DeMeo et al. (2009) to derive H_V for the system.

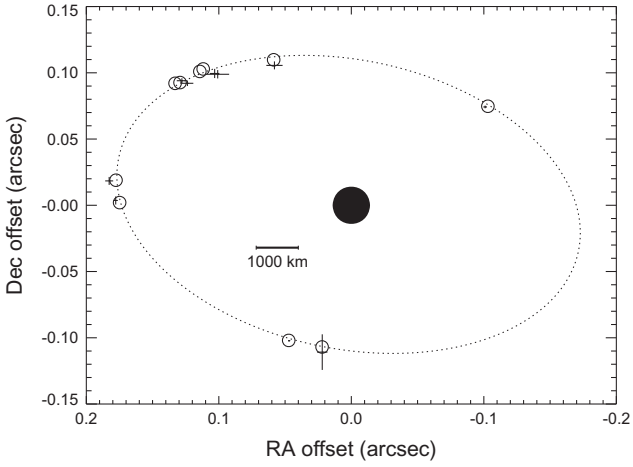

Fig. 2. Observed sky-plane positions of the secondary of (120347) Salacia–Actaea relative to primary are shown as points with RA and Dec error bars (error bars are sometimes smaller than the symbols). The fitted orbit is shown as a dotted oval projected for the geometry of the mean time of the observations. The open circles show the position of the secondary at the actual times of the observations as predicted from the fit (*i.e.* the offset between the observed and modeled positions is the distance between the 'plus' symbols formed by the error bars and the centers of the open circles). The symbol sizes are scaled to reflect both the relative sizes of the components (based on the measured magnitude difference and the assumption of equal albedos), and their absolute size relative to the orbit (as determined from the *Spitzer* measurements discussed below).

for Typhon, acquired under program 55, were presented by Stansberry et al. (2008), and utilized by Grundy et al. (2008) in determining a density for the Typhon system.) Both targets were observed using the photometry template, tailored for point sources. Salacia was targeted twice, with both 24 and 70 μm data collected during each of those visits. Typhon was targeted twice, with 24 and 70 μm data collected during the first visit, and only 24 μm data taken on the second visit (the earlier 70 μm data were of high quality, so a second 70 μm observation was deemed unnecessary). Fig. 3 shows the images of both objects derived from the above observations.

The data were reduced using the MIPS instrument team data analysis tools (Gordon et al., 2005) to produce flux-calibrated images for each band and each visit. Further processing was performed in order to subtract away the contribution from background objects, as described in Stansberry et al. (2008). These "sky-subtracted" images for each target were then coadded in the co-moving frame of the target to produce final images with the best possible signal-to-noise ratio (SNR). Aperture photometry was performed on the original, intermediate, and final images to confirm the consistency of the measured fluxes. We applied aperture corrections as given in Gordon et al. (2007) and Engelbracht et al. (2007) to arrive at the final in-band flux values. Finally, we color-corrected the in-band fluxes (Stansberry et al., 2007) to obtain monochromatic flux densities. Table 4 gives the in-band fluxes, SNR and observational circumstances for each observation, and the final adopted values derived from both epochs for each target. Monochromatic flux densities and uncertainties are given in Table 5.

4. Thermal modeling

While there are several flavors of thermal models used to determine diameters of airless bodies, all rely on the same basic principle. The thermal flux is proportional to the target's cross-sectional

Table 3
Orbital parameters and system mass for (120347) Salacia–Actaea.

Parameter	Symbol	Orbit 1 (χ^2 = 26.2)	Orbit 2 (χ^2 = 26.2)
Orbital elements[a]			
Period (days)	P	5.493863 ± 0.000095	5.493724 ± 0.000079
Semimajor axis (km)	a	5570 ± 40	5666 ± 41
Eccentricity	e	0.0124 ± 0.0036	0.0044 ± 0.0035
Inclination[b] (deg)	i	124.28 ± 0.39	23.45 ± 0.40
Mean longitude[b] at epoch[c] (deg)	ε	323.22 ± 0.93	303.83 ± 0.34
Longitude of asc. node[b] (deg)	Ω	81.92 ± 0.67	48.3 ± 1.2
Longitude of periapsis[b] (deg)	ϖ	285 ± 16	221 ± 19
Derived Parameters			
System mass (10^{20} kg)	M_{sys}	4.537 ± 0.098	4.776 ± 0.104
GM_{sys} (km^3 day^{-2})	μ	30.28 ± 0.65	31.88 ± 0.70
Orbit pole right ascension[b] (deg)	α_{pole}	351.92 ± 0.67	318.3 ± 1.2
Orbit pole declination[b] (deg)	δ_{pole}	−34.28 ± 0.38	66.55 ± 0.59
Orbit pole ecliptic longitude (deg)	ϕ_{pole}	338.00 ± 0.62	22.3 ± 1.9
Orbit pole ecliptic latitude (deg)	λ_{pole}	−28.07 ± 0.40	71.26 ± 0.45
Next mutual event season		2067	2111

[a] Elements are for secondary relative to primary. The average sky plane residual is 0.5 mas for both orbits.
[b] Referenced to J2000 equatorial frame.
[c] The epoch is Julian date 2454300.0 (2007 July 18 12:00 UT).

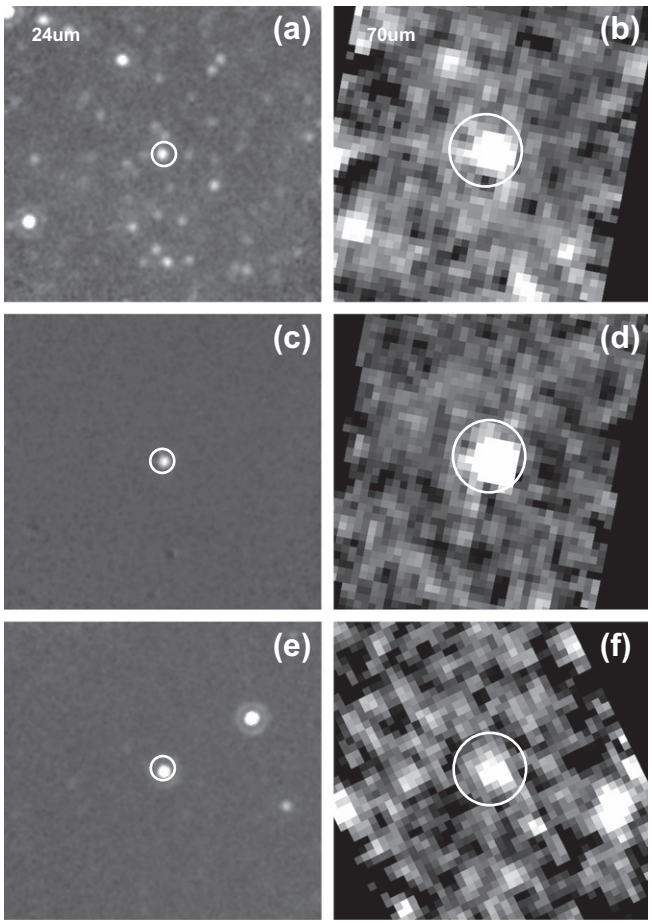

Fig. 3. *Spitzer* images of Salacia (panels a–d) and Typhon (panels e–f) in the 24 μm (left side) and 70 μm (right side) bands. Panels a and b show the data for Salacia resulting from a single observation. Panels c and d show the final product, including sky-subtraction and coadding the two observations. Panels e and f show the data for Typhon resulting from a single observation (*i.e.* no sky-subtraction). Circles are centered at the target ephemeris position, and have radii of 8″ (24 μm) and 24″ (70 μm). The pixel scales for the two MIPS bands are 2.49″ (24 μm) and 9.85″ (70 μm); in these images the pixels have been re-sampled and are half as large.

area and (approximately) the Planck function at the surface temperature and the observed wavelength. A single thermal measurement can be combined with the visual magnitude to distinguish between a small, high-albedo (*i.e.* cool) object and a larger, low-albedo (*i.e.* warm) object. A more robust determination of the size can be made if the thermal data directly constrain the temperature of the surface (as our MIPS data do) by measuring the color temperature of the emission. Then the thermal data alone give the size of the target, and the visual magnitude really only matters for determining the albedo. Systematic and model-dependent uncertainties on both the size and albedo are significantly reduced in this case. Additionally, data that measure the color temperature (as our MIPS data do for TNOs) can also be used to place constraints on the thermal inertia. This follows because for a given albedo, a low-thermal inertia surface will have higher dayside temperatures than one with a high thermal inertia. Alternatively, data such as we present here can be used to constrain an empirical factor that adjusts the dayside temperature (see discussion of the "beaming parameter" below).

Table 5
Spitzer color temperatures and monochromatic flux densities.

	(120347) Salacia	(42355) Typhon	Units
F_ν (23.68 μm)[a]	0.546 ± 0.021	5.09 ± 0.16	mJy
F_ν (71.42 μm)[a]	36.6 ± 3.7	25.8 ± 4.6	mJy
24:70 μm color Temp.[b]	54.3 ± 1.0	84.0 ± 3.9	K

[a] The effective wavelengths for the MIPS 24 and 70 μm channels. Uncertainties given here include that on the absolute calibration.
[b] Color-corrections are calculated for a blackbody spectrum at this temperature. The corrections and color temperature are solved for iteratively.

With the diameter in hand, it is simple to determine the albedo from the visual magnitude. The geometric albedo, p_V, and diameter, D, are related via (*e.g.* Russel, 1916; Harris, 1998) $Dp_V^{1/2} = D_0 10^{-H_V/5}$, where H_V is the absolute magnitude of the object (see Table 2), and $D_0 = 2\ \mathrm{AU}\ 10^{V_\odot/5}$. Recent work on absolute flux calibration has resulted in a slightly updated value for the apparent magnitude of the Sun, $V_\odot = -26.74$ (*e.g.* Rieke et al., 2008), resulting in $D_0 = 1342$ km (earlier works had $D_0 = 1329$ km). Note also that the ratio of the visual geometric albedo to the bolometric albedo is $A_B = qp_V$, where q is the phase integral. Bowell et al. (1989) show that for a wide range of low to moderate albedo asteroids, $q = 0.39$. Brucker et al. (2009) also find that low-albedo icy objects in the outer Solar System also have phase integrals of about 0.39, so we assume that value here. This is justified *post-facto* by our finding that the albedos of both objects are indeed quite low.

We employ three different thermal models to derive diameters and albedos from the *Spitzer* data. Two are a modified version of the Standard Thermal Model (STM), and the Isothermal Latitude Model (ILM), which are described in detail by Lebofsky et al.

Table 4
Spitzer observations.

Observation date[a] UT	r[b] (AU)	Δ[b] (AU)	Band[c] (μm)	S/N[d]	Flux[c] (mJy)
(120347) Salacia					
2006/12/03 15.350[h]	43.8192	43.3758	24	24	0.573
2006/12/03 15.653[h]	43.8192	43.3760	70	17	30.2
2006/12/03 8.449[h]	43.8197	43.4005	24	26	0.597
2006/12/03 8.752[h]	43.8197	43.4007	70	17	36.7
Adopted value	43.8195	43.3883	24		0.585 ± 0.014
Adopted value	43.8195	43.3883	70		32.8 ± 2.7
(42355) Typhon					
2008/06/26 4.997[h]	17.6781	17.4987	24	89	4.72
2008/06/26 5.331[h]	17.6781	17.4989	70	6	23.9
2008/06/27 15.682[h]	17.6787	17.5232	24	91	5.03
Adopted value	17.6783	17.5069	24		4.88 ± 0.05
Adopted value	17.6783	17.5069	70		23.9 ± 4.2

[a] Dates are average UT mid-times of observations at the location of the observer (Spitzer).
[b] The distance from the Sun to the target is r and from the observer to the target is Δ. Phase angles for these observations were all <2°.
[c] The MIPS bands are referred to as 24 and 70 μm. Fluxes are raw, in-band values: for monochromatic fluxes and wavelengths, see Table 5. Individual contributions from the components of the binary systems are not spatially resolved in the *Spitzer* data.
[d] The signal to noise ratio of the individual detections is given. These values do not include uncertainties in the absolute calibration, nor do the error bars for the Adopted Values.

(1986) and Spencer et al. (1989, where the ILM is called the fast rotator model). Third is thee Thermophysical Model (TPM), described in detail by Spencer (1990). By employing several models we quantify the systematic effects of the different model assumptions on the derived physical parameters. Next we briefly summarize those assumptions for the three models.

The STM assumes a surface with zero thermal inertia: the temperature at points on the dayside is computed by equating the absorbed insolation with the emitted thermal radiation. Nightside temperatures are set to zero. The temperature distribution in the STM is azimuthally symmetric about the subsolar point, and independent of the orientation of the rotational pole. The ILM assumes infinite thermal inertia, such that dayside and nightside temperatures at a given latitude are equal. The ILM temperature distribution is azimuthally symmetric about the rotational axis. Many studies assume equatorial illumination, but it is simple to allow other illumination geometries, as we do here. Note that in the limit of illumination at the pole the STM and ILM predict the same spectrum. For a given set of observing circumstances, and the same albedo and emissivity, the STM predicts higher fluxes and a hotter spectrum, and the ILM a cooler, fainter spectrum. We employ a slight variant of the STM, the Near Earth Asteroid Thermal Model (NEATM; Harris, 1998), which accounts for the non-zero phase angle of the observations, by performing the appropriate integral over the visible portion of a target's surface. (We also include this effect in our implementation of the ILM.) The NEATM also allows the beaming parameter (see next paragraph) to be a parameter of the fit, as did the hybrid-STM used to model TNOs by Stansberry et al. (2008) (the hybrid-STM, however, assumes a phase angle equal to zero). For observations of the very distant objects we are discussing here, the differences between the NEATM and STM/ILM are inconsequential. We will refer to the model results via the acronyms STM and ILM for simplicity and to distinguish between cases with zero and infinite thermal inertia.

One feature of the STM (and the ILM, as we implement it) that merits brief discussion is the "beaming parameter," η, originally introduced to account for seemingly elevated dayside temperatures of main-belt asteroids (*e.g.* Lebofsky et al., 1986). η affects the STM spectrum by modifying the subsolar-point temperature, $T_{SS}^4 = S_0(1-A_B)/(\epsilon\sigma\eta)$, where S_0 is the solar flux impinging on the target, A_B is the bolometric albedo, ϵ is the emissivity and σ the Stefan–Boltzmann constant: for $\eta < 1$ dayside temperatures are elevated. However, in many cases thermal observations of asteroids require $\eta \geqslant 1$ (*e.g.* Harris, 1998; Fernández et al., 2003; Delbó et al., 2003). Stansberry et al. (2008) found that for TNOs η is typically in the range 1–1.5, indicating that dayside temperatures are lower than would result from instantaneous equilibrium. Lower dayside temperatures would be expected, for example, if the surface has non-zero thermal inertia. In summary, η can be thought of as a free parameter for the STM and ILM which allows the color of the model's thermal emission to be tuned to match the observed color of the emission from the target. If the models are tuned in that way, the STM and ILM give diameters that are very similar, and that are also in excellent agreement with the diameter given by the TPM. This agreement was explored in considerable detail for TNOs by Brucker et al. (2009), who concluded that the STM had marginally better agreement with TPM results than did the ILM.

The TPM solves the time-dependent thermal conduction equation, tracking heat conducted into and out of the subsurface. At the surface, forcing is provided by the temporally and spatially varying insolation, and the thermally-radiating boundary condition is applied. Surface (and sub-surface) temperatures depend on the conductivity, mass density, and heat capacity of the subsurface material (combined into the thermal inertia $\Gamma = \sqrt{\kappa\rho c_p}$, where κ is the thermal conductivity, ρ is the mass density, and c_p is the specific heat). The TPM also accounts for the effects of pole orientation and rotation period (P). The period appears in the solutions in combination with the thermal inertia as the thermal parameter (Spencer, 1990), $\Theta = \Gamma/\left(\sqrt{P/2\pi}\epsilon\sigma T_{ss}^3\right)$, where ϵ is the emissivity and T_{ss} the sub-solar equilibrium surface temperature. Θ is the ratio of the radiative cooling timescale to the diurnal timescale, and so characterizes the amplitude of diurnal temperature variations.

The TPM also includes the effects of surface roughness, parameterized in terms of the rim angle, θ, of circular craters/depressions, and the fractional coverage of such depressions on the surface. Very shallow depressions have θ approaching 0°, while hemispherical ones have $\theta = 90°$. Such depressions are warmer than a smooth surface due to internally reflected sunlight getting additional opportunity to be absorbed, and self-radiation between the walls and floor of the depression. The magnitude of the effect of the depressions on the thermal spectrum is also determined by the fraction, f, of the surface they cover. Müller et al. (1999) used an extensive *Infrared Space Observatory* (ISO) data set to characterize the typical values of Γ, θ and f for main-belt asteroids, finding values of 15 J m^{-2} s$^{-1/2}$ K^{-1}, 73° and 0.6, respectively (where we have translated their RMS slope of 0.7 into an opening angle). Spencer (1990) summarizes how the above realization of roughness in the TPM relates to the empirical beaming parameter (η) of the STM. He also shows that the effects of surface roughness and thermal inertia counter-act each other, so that the observed emission results from a combination of their effects. This explains why η can take on values ranging from <1 (roughness/beaming dominated) to >1 (thermal-inertia dominated). In general he demonstrates that roughness-induced beaming is more important for surfaces with small Θ (*i.e.* large diurnal temperature variations).

4.1. STM and ILM results for Salacia and Typhon

Fig. 4 shows fits of the STM/NEATM to the *Spitzer* fluxes of Salacia and Typhon. ILM fits to the data (not shown) are very similar, having slightly higher fluxes longward of 100 μm. We also ran the ILM for two cases: equatorial illumination, and illumination under the assumption that the rotational poles of the components of the target are aligned with the orbital angular momentum of the binary orbit (as would be the case for a fully tidally-evolved system). Fitted values for the diameters, geometric albedos, and beaming parameter for both objects are summarized in Table 6, with results given for both thermal models. We estimate the range of acceptable fits to the data by separately fitting models to the $\pm1\sigma$ flux values (indicated by the broken lines in the figure). Overall agreement between the model results is good, indicating that the different assumptions embodied in those models do not contribute to large differences in the derived physical parameters. However, it is apparent that the equatorially-illuminated ILM fits give slightly larger diameters (and smaller albedos) than do the STM fits to the same data.

The uncertainties on the derived parameters D and p_v are correlated, a fact that is not captured when the uncertainties are stated as above. One way to illustrate the allowed values and their relationship is to plot contours of χ^2, as shown in Fig. 5. Here we ran a grid of STM models, computing the χ^2 statistic for each. The extrema of the 1σ contours are quoted in Table 6 as our adopted limits on D and p_V. However, it should be noted that any particular value of D within the quoted range cannot be associated with all values of p_V within the range, nor *vice versa*.

4.2. Thermophysical modeling

Thermophysical models were computed on a grid of assumed values for the thermal inertia, $0.1 \leqslant \Gamma \leqslant 40$ J m^{-2} s$^{-1/2}$ K^{-1}. This range of Γ spans the lowest-plausible values up to that of the dark

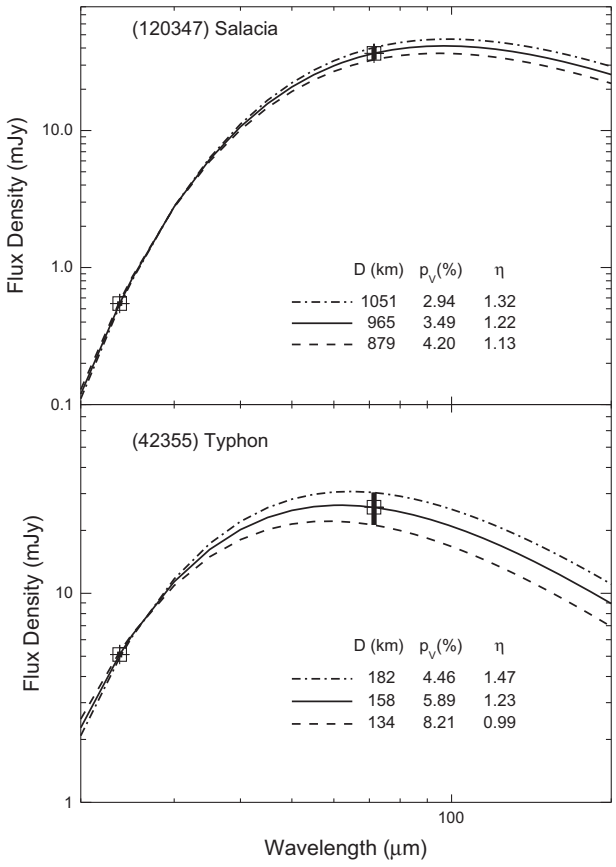

Fig. 4. STM fits to the *Spitzer* observations of Salacia (top) and Typhon (bottom). Thick vertical error bars show the uncertainties on the flux densities. Uncertainties in the fitted parameters are derived from fitting the upper and lower bounds on the flux densities; the range in the fitted parameters is summarized in the legend. The best-fit blackbody spectrum is also shown (nearly indistinguishable from the best-fit model). ILM and TPM fits to the data give very similar results (see Table 6).

Table 6
Spitzer color temperatures and monochromatic flux densities.

Object	Thermal Model[a]	D_{Eff}[b] (km)	p_V[c] (%)	η_{STM}[d]	Γ_{TPM}[d]
(120347) Salacia					
	STM	965 ± 86	$3.49^{+0.71}_{-0.55}$	1.22 ± 0.10	
	STM_{Stat}	974 ± 109	$3.43^{+0.83}_{-0.66}$	1.23 ± 0.12	
	ILM_{Eq}	919 ± 81	$3.85^{+0.78}_{-0.60}$		
	ILM_{Pole}	975 ± 87	$3.42^{+0.70}_{-0.54}$		
	Adopted[e]	954 ± 109	$3.57^{+1.03}_{-0.72}$		
	TPM	1120 ± 220	$2.6^{+1.2}_{-0.8}$	0.4 – 30	
(42355) Typhon					
	STM	158 ± 24	$5.89^{+2.32}_{-1.43}$	1.23 ± 0.24	
	STM_{Stat}	159 ± 34	$5.93^{+3.41}_{-1.80}$	1.24 ± 0.31	
	ILM_{Eq}	154 ± 24	$6.24^{+2.42}_{-1.51}$		
	ILM_{Pole}	161 ± 25	$5.72^{+2.27}_{-1.40}$		
	Adopted[e]	157 ± 34	$6.00^{+4.10}_{-2.08}$		
	TPM	157 ± 25	$5.9^{+2.3}_{-1.5}$	0.2 – 30	

[a] Model used: Standard Thermal Model (STM); Monte-Carlo STM (STM_{Stat}); Isothermal Latitude Model with equatorial illumination (ILM_{Eq}); Isothermal Latitude Model assuming the rotational pole is parallel to the binary-orbit pole (ILM_{Pole}); and Thermophysical Model (TPM).

[b] Effective diameter, i.e. the diameter of a single body with the same projected area as the combined components of the binary.

[c] Effective geometric albedo, i.e. the albedo obtained by combining D_{Eff} with the system- integrated absolute magnitude.

[d] The beaming parameter, η (dimensionless), is given for the STM, and the thermal inertia, Γ (J m$^{-2}s^{-1/2}K^{-1}$), is given for the TPM. Beaming parameters are typically quoted in the context of the STM; for consistency with other studies, we don't quote the values for our ILM fits.

[e] The adopted values are based only on the STM and ILM results for consistency with previous studies based on Spitzer and Herschel observations of TNOs.

regions on Pluto (Lellouch et al., 2011). Pluto's atmosphere contributes to the conductivity in sub-surface pores there, resulting in a higher value of Γ than on airless bodies (such as Salacia and Typhon). Our adopted upper limit also approaches that of the lunar regolith, and includes the typical asteroidal value, 15 J m^{-2} s$^{-1/2}$ K^{-1}, noted earlier. Also, Γ is a increasing function of temperature (due primarily to decreased conductivity), so it would be unexpected to find TNOs with higher values of Γ than that of the Moon. Further, for other TNOs where Γ has been constrained, it is generally found to be < 5 J m^{-2} s$^{-1/2}$ K^{-1} (Müller et al., 2010; Lim et al., 2010; T. Müller, personal communication).

Sub-solar latitudes were chosen as 0° (equatorial illumination, giving the least STM-like temperature distribution), and to include the possibility that the rotational poles are aligned with the angular momentum vector of the binary orbits. For both objects a sub-solar latitude of 40° approximates the latter case. For larger sub-solar latitudes, the TPM temperature distribution begins to resemble that of the STM. The surface roughness cases we consider cover the plausible range (Müller et al., 1999), and include the roughness they found for typical asteroids. Following Spencer (1990), we parameterize the roughness in terms of f, the fractional coverage of craters, and θ, the interior rim angle (where $\theta = 90°$ is a hemispherical bowl). The specific cases we consider are: (1) no roughness ($f = \theta = 0$), (2) low roughness ($\theta = 60°, f = 0.4$), (3) nominal/asteroidal values ($\theta = 73°, f = 0.6$), and (4) high roughness ($\theta = 76°, f = 1.0$).

The final assumption necessary for the TPM is the rotation rate. Rotation periods shorter than about 3 h are implausible, implying either a strongly triaxial shape (and correspondingly large-amplitude lightcurve) while 20 h is comparable to the longest known TNO rotation period (Sheppard et al., 2008), other than Pluto and, perhaps, Eris (Maris and Carraro, 2008) These rotation periods also encompass the tentatively-identified Salacia rotation periods (noted in the introduction). For Typhon the question is whether the lightcurve is single or double-peaked, so we consider rotation periods of 9 and 20 h to encompass those possibilities.

For each combination of the parameters just discussed, we varied D and p_V to find the model that best fit our data, and including the uncertainties on the thermal fluxes and the absolute magnitudes. In most cases the resulting fits were quite poor, having χ^2 values far above unity. Below we summarize the fitted TPM model parameters that provided acceptable fits to the data, and compare those to the earlier values we adopted based on our STM and ILM model fitting (in the next two sections we use the term "STM" to encompass both flavors of model).

4.2.1. TPM results for Salacia

Fig. 6 summarizes the TPM modeling results for Salacia (see also Table 6). We plot only those solutions where $\chi^2 \leqslant 1$. (Because the TPM has more parameters than we have data points with which to constrain the models, acceptable fits have $\chi^2 \leqslant 1$.) The TPM results are consistent with the very low albedo and large size we determined earlier, but formally result in significantly larger uncertainties: $895 \leqslant D \leqslant 1335$ km and $1.8 \leqslant p_V \leqslant 3.8\%$. Much of the additional uncertainty is due to the inclined (*i.e.* those where we assumed the rotational pole and binary orbit poles were parallel), 3-h rotation models. The model with low roughness adds significantly to both the magnitude of the uncertainty and the bias to larger sizes and lower albedos than adopted based on the STM results.

If we focus on the models with $\Gamma \leqslant 10$ J m^{-2} s$^{-1/2}$ K^{-1}, the ranges for diameter and albedo are both narrower and in better

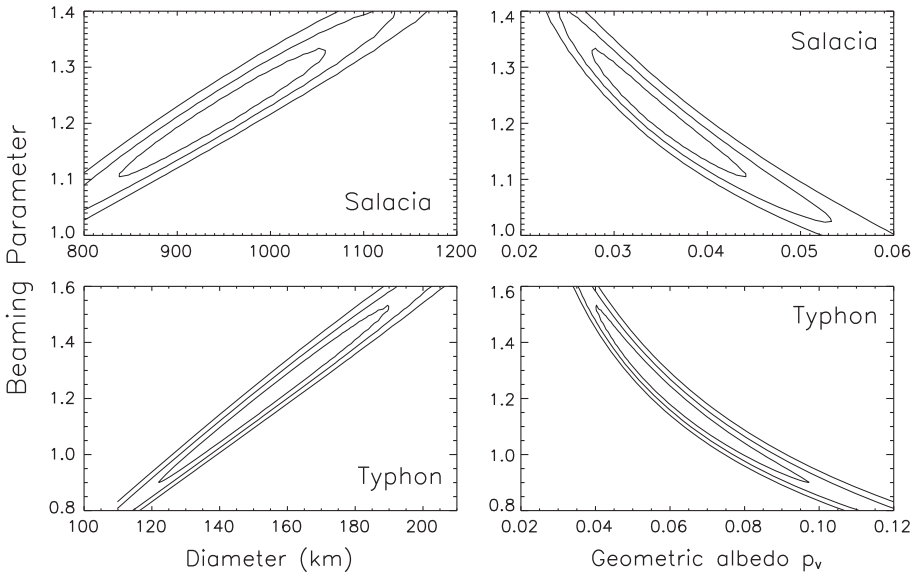

Fig. 5. Contours of χ^2 resulting from fits of the STM to our *Spitzer* data. Models were run on a D *vs.* η grid; p_V is derived from D via the absolute visual magnitude. Contour levels are at significance levels equivalent to 1, 2 and 3σ. The 1σ contours give limits on D and p_V that are consistent with the STM fits shown in Fig. 4, but additionally illustrate the correlated uncertainties on the physical parameters resulting from the fits.

agreement with those from the STM: $910 \leqslant D \leqslant 1200$ km and $2.2 \leqslant p_V 3.7\%$. If, as noted above, Γ is closer to the very low values found for other TNOs, the TPM results are in excellent agreement with those from the STM. Because the *Spitzer* data provide a very tight constraint on the color temperature of the emission from Salacia (Table 5), the STM results are likely to be quite accurate. Thus, while we cannot formally rule out the larger sizes and lower albedos resulting from our TPM models for Salacia, it seems likely that it has a very low thermal inertia, and a size and albedo consistent with the values we adopted from the STM results.

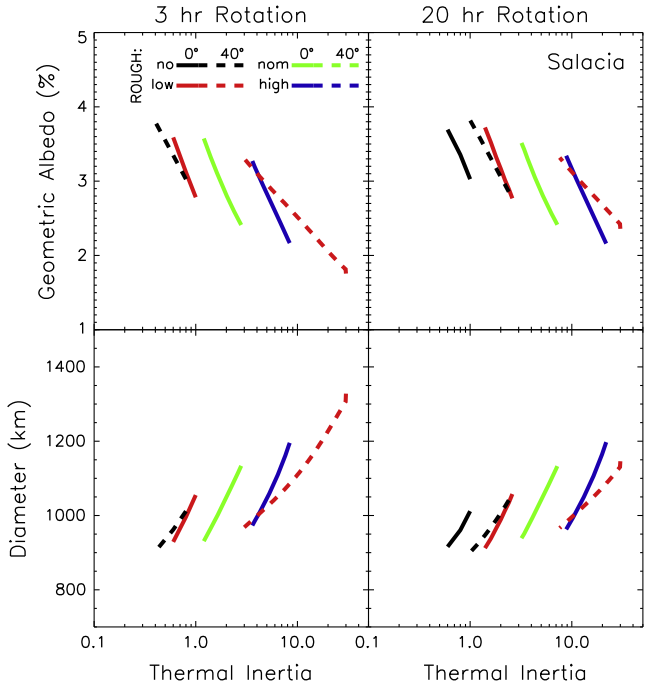

Fig. 6. Thermophysical model results for Salacia. Albedo (top panels) and diameter (bottom panels) *vs.* thermal inertia, and for assumed rotation periods that bracket the likely period (3 h: left panels, 20 h: right panels). The grid of models also included two assumptions for the sub-solar latitude: 0° (solid lines) and 40° (dashed lines). Surface roughness was allowed to range from a smooth surface (no roughness: black lines), low roughness (red lines), nominal roughness (green lines) and very rough (blue lines). Curves are plotted for the range of models giving reduced $\chi^2 \leqslant 1$.

4.2.2. TPM results for Typhon

Fig. 7 summarizes the TPM modeling results for Typhon (see also Table 6). Unlike the situation for Salacia, our data do not meaningfully constrain the thermal inertia for Typhon: the entire range, $\Gamma = 0.2$–30, is allowed. The TPM models do seem to favor a sub-solar latitude near the equator. For the higher-latitude illu-

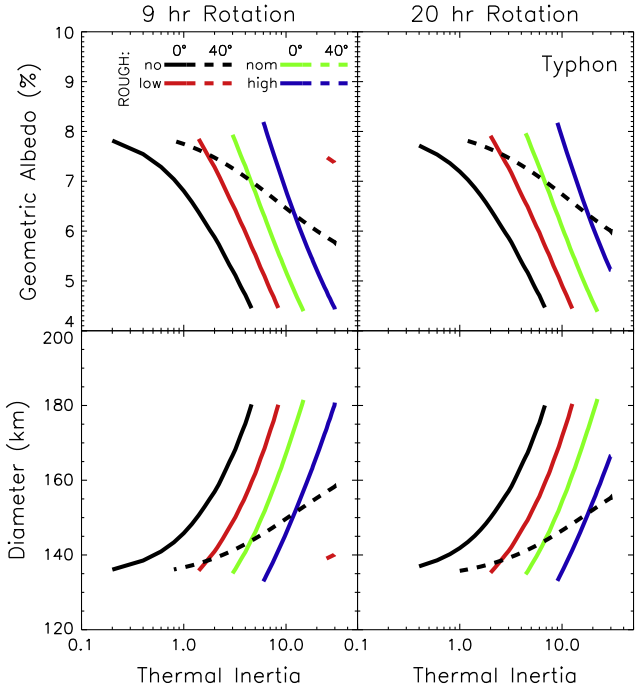

Fig. 7. Thermophysical model results for (42355) Typhon. Symbols are the same as for Fig. 6, but the two rotation periods considered are 9 and 20 h.

mination cases, only the zero roughness models provide an adequate fit to the data.

In contrast to the case for Salacia, here the TPM and adopted STM results are in excellent agreement. The TPM does favor slightly lower albedos than the full range of the adopted values, but we note that for the actual STM row in Table 6 the maximum albedo is 8.2%, exactly the value for the TPM. Thus, it may be that the TPM results are suggesting that the temperature distribution on Typhon is more STM-like than ILM-like. The close agreement of the STM and TPM solutions may be telling us that the albedo is <8.2%, even though our adopted values allow solutions for albedos as high as 10%.

5. Density results

The densities of (120347) Salacia–Actaea $\left(1.16^{+0.59}_{-0.36}\right)$ and (42355) Typhon–Echidna $\left(0.60^{+0.72}_{-0.29}\right)$ are given in Table 7 (along with the component sizes) while Fig. 8 plots them in the context of the other binaries with measured densities (references for these values are given in the Introduction). For all objects (except Pluto, where the size and density of the satellite has been independently determined), we have assumed that the albedos, bulk composition and porosity of the components of a system are equal. Expressions for the component diameters and system density under these assumptions are given in, for example, Stansberry et al., 2006. The number of density determinations remains small, but these initial results indicate a clear relationship between density and diameter. (47171) 1999 TC_{36}, (65489) Ceto, (26308) 1998 SM_{165}, and Typhon all cluster at densities between 0.5 and 0.8 g/cm^3. The densities of Salacia and Orcus are very similar to one another, and are intermediate between those of the small TNO binaries and the dwarf-planets Pluto-Charon, Eris and Haumea. We include Varuna in the figure even though it is not a binary (using the lower-limit density from Jewitt and Sheppard (2002)). Based on the *Spitzer* results ($D = 500 \pm 100$ km, $p_V = 16 \pm 9\%$, Stansberry et al., 2008), Varuna nicely fills the gap between the smaller TNOs and Salacia and Orcus. More recent Herschel observations (T. Müller, personal communication) give a diameter and albedo consistent with those from *Spitzer*. (Submillimeter results for Varuna (Jewitt et al., 2001; Lellouch et al., 2002; Altenhoff et al., 2004) indicate $D \simeq 1000$ km, $p_V \simeq 6\%$ for Varuna, but such a large size and low albedo would have resulted in fluxes in the *Spitzer* and Herschel bands about four times larger than the observed fluxes.)

Table 7
Mass densities and component sizes.

Object	$D_{primary}$[a] (km)	$D_{secondary}$[a] (km)	ρ[a] (g cm^{-3})
Salacia–Actaea	905 ± 103	303 ± 35	$1.16^{+0.59}_{-0.36}$
Typhon–Echidna	137 ± 30	77 ± 16	$0.60^{+0.72}_{-0.29}$

[a] Component diameters assuming equal albedos.

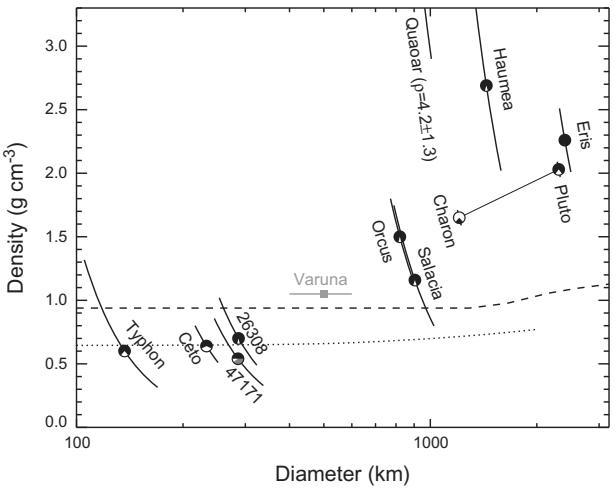

Fig. 8. The known densities of binary TNOs and Centaurs (circles) and Varuna (square – lower limit from Jewitt and Sheppard (2002)) are plotted *vs.* object radius. Our results for Salacia make it the largest such object with a density less than 1.5 g/cm^3, while Typhon is confirmed as one of the small, very low density objects. The dashed line is the theoretical bulk density for a pure H_2O ice sphere subject to self compression; the dotted line is for granular ice I_h, also including self-compression (McKinnon et al., 2005). References for the densities are given in the Introduction, although we have recomputed Haumea's using recent Herschel results for its dimensions (Lellouch et al., 2010).

The other objects in Fig. 8, Quaoar and the dwarf planets Pluto-Charon, Eris, and Haumea, are systematically more dense. Quaoar, with nearly the same diameter as Orcus and Salacia, has the highest measured density of any TNO (Fraser and Brown, 2010; although more recent stellar occultation (Braga-Ribas et al., 2011) and Herschel (Kiss et al., 2011) results suggest a density below 3 g/cm^3). Fig. 8 also illustrates the satellite – primary magnitude difference for each system. Eris ($\delta m = 6.7$) and Quaoar ($\delta m = 5.6$) have much fainter satellites than Salacia, Orcus and the small binaries. Haumea's satellite, with $\delta m = 3.1$, is relatively bright, but still fainter in relative terms than the satellites of the smaller objects (26308) (1998 SM_{165}, with $\delta m = 2.7$, has the relatively smallest satellite of that group). As for Pluto-Charon (Canup, 2011), many aspects of the Haumea system have been attributed to a massive collision (*e.g.* Ragozzine and Brown, 2009). As summarized in Section 6, the Quaoar and Eris systems also probably formed in large collisional events; if so, then all 4 of the highest-density TNO systems are products of massive collisions. The fact that the smaller TNO binaries are lower density, and tend to have relatively larger satellites (*e.g.* Grundy et al., 2011; Parker et al., 2011; Sheppard et al., 2012), as can be seen from the figure, is a clue that they may have formed differently. This possibility is also supported by dynamical models (Parker and Kavelaars, 2012) indicating that the binaries of the cold-classical population may have formed in situ very early in Solar System history.

The small objects ($D < 500$ km) have densities less than the bulk density of pure water ice, but roughly consistent with a pure water ice composition if the ice is porous. The larger TNOs (Salacia and Orcus) have densities a bit higher than that of water ice, suggesting that they probably contain some denser (presumably silicate) material. Given that water–ice is evident in the spectrum (*e.g.* Barucci et al., 2008b) of high-albedo Orcus (Lim et al., 2010) but not Salacia (Schaller and Brown, 2008), and their very similar densities, it appears that TNOs with very similar bulk composition can have very dissimilar surfaces. There is no particular reason to expect that the smaller objects would not contain about the same fraction of silicates as the larger ones, and the presence of some silicates is expected on cosmochemical grounds. Stansberry et al. (2006) explored the implications of a water plus silicate composition for the interior structure (porosity) of (47171) 1999 TC_{36}. It is now known that 1999 TC_{36} is indeed a triple with the "primary" consisting of two nearly equal-sized components (Benecchi et al., 2010). Their updated mass for the system implies a density of $0.54^{+0.32}_{-0.21}$ g/cm^3. If the bulk density of the water plus silicates making up 1999 TC_{36} is taken to be 1.5 g/cm^3, their density implies a porosity in the range 0.43–0.78. Our density for Typhon implies a very similar range of porosity, 0.33–0.73. As noted by Stansberry et al. (2006), porosities greater than about 0.36 require unusual, strength-supported interior structure. The size they computed for gravitational self-compaction of an icy sphere (assumed density of 1 g/cm^3), $D_{SC} \simeq 330$ km, is larger than the components of Typhon

(and 1999 TC_{36}), so such large porosities are at least plausible for these objects.

Salacia is much larger than the self-compaction size, and so is unlikely to have significant interior void space. It is also large enough that it is probably differentiated, so we examine the implications of models with a rocky core (assumed density in the range 2.77–3.66 g/cm^3, *e.g.* Stansberry et al., 2006) and a water ice mantle having zero or 10% porosity. For the non-porous mantle we find that Salacia could have a rocky core with a diameter as large as 0.4 the total diameter (if the true density is our best-estimate value) or as large as 0.65 the total diameter (if the true density is our upper-limit value). These configurations have corresponding rock/ice mass ratios 0.2–1.1 (for a silicate density of 3.0 g/cm^3). If the mantle is allowed to be 10% porous, our best-estimate and upper-limit densities allow for slightly larger cores, with diameters as large as 0.45 and 0.7 of the overall radius (implying slightly higher rock/ice mass ratios). If the rock/ice mass ratio of Pluto (roughly unity, McKinnon et al., 1997) is a guide to what we should expect for Salacia, then the true density must be near the upper end of the range we find. Since the uncertainty in our density is dominated by the uncertainty in the diameter, not the mass, this would further imply that D is near the lower bound we find, and p_V near the upper bound.

6. Discussion

6.1. (120347) Salacia

Salacia is not the only low-albedo TNO with a diameter near 1000 km. Hot-classical TNO 2002 MS_4 ($D = 934 \pm 34$ km, $p_V = 5.1^{+0.4}_{-0.3}\%$, Vilenius et al., 2012) and Plutino 208996 (2003 AZ_{84}) ($D = 910 \pm 60$ km, $p_V = 6.5^{+2.5}_{-1.5}\%$, Müller et al., 2010; Mommert et al., 2012) are rather similar. However, classical Quaoar is of comparable size ($D = 890 \pm 70$ km), but has an albedo in excess of 15% (Fraser and Brown, 2010), while hot-classical 55565 (2002 AW_{197}) ($D = 740 \pm 110$ km) has $p_V = 12^{+4}_{-3}\%$ (Cruikshank et al., 2005; Stansberry et al., 2008), and 90482 Orcus ($788 \leqslant D1010$ km) has $0.32 \geqslant p_V \geqslant 25\%$ (Lim et al., 2010; Brown et al., 2010). These higher-albedo objects all have evidence for water ice in their near-IR spectra, but so does 2003 AZ_{84} (see Barucci et al., 2008a and references therein). The spectra of Salacia (Schaller and Brown, 2008; Trujillo et al., 2011) and 2002 MS_4 (Trujillo et al., 2011) do not indicate the presence of water ice. Thus there is no clear pattern that emerges regarding the albedos and composition of objects in the 700–1000 km size class. On the other hand, TNOs larger than 1000 km, Eris, Makemake, Haumea (Sicardy et al., 2011; Lim et al., 2010; Lellouch et al., 2010) and Pluto all have geometric albedos in excess of 50%, and spectroscopic evidence for abundant ices. Perhaps objects somewhat smaller than these are in an intermediate size range where evolutionary processes can lead to either high or low albedo, with the outcome depending on details of the history of individual objects.

Salacia has been rejected as a member of the Haumea collisional family (Brown et al., 2007; Ragozzine and Brown, 2007; Schaller and Brown, 2008; Snodgrass et al., 2010; Trujillo et al., 2011) based on its lack of detectable water–ice absorption features. Our results provide an independent test of the hypothesis that all Haumea family members have such absorptions. The albedos (where they are known) of accepted (*i.e.* icy) Haumea family members are diverse, ranging from about 12% (2002 AW_{197}) (Stansberry et al., 2008) to around 80% for Haumea, and 88% for (55636) 2002 TX_{300} (Elliot et al., 2010). Had we discovered a moderate or high albedo for Salacia, that might have suggested that its membership in the family be reconsidered. Salacia is extremely large to have been produced (and ejected onto an un-bound orbit) during the Haumea-family forming collision: it is 0.7 times as large as Haumea (Lellouch et al. (2010) give Haumea's effective diameter as 1317 km), and Salacia's mass is 1/10 that of Haumea's. The relatively large size of Salacia's satellite is consistent with capture or co-accretion, so suggests a non-collisional origin (unless it formed in a scenario similar to Pluto–Charon). Taken together, these (and the lack of water–ice features) strongly suggest that Salacia is not a member of the Haumea collisional family.

6.2. (42355) Typhon–Echidna

Our new *Spitzer* results for Typhon ($D = 157 \pm 34$ km, $p_V = 6.00^{+4.10}_{-2.08}\%$) largely confirm the previously determined albedo $\left(p_V = 5.1^{+1.3}_{-0.9}\%\right)$ and diameter $D = 175 \pm 19$ km (Stansberry et al., 2008). The new detection at 24 μm confirms that the beaming parameter for Typhon, assumed to be 1.2 in that study, is indeed very close to that value, thus the good agreement in the other physical parameters. Müller et al. (2010) find similar values ($p_V = 7.2^{+1.3}_{-0.7}\%$, $D = 144 \pm 10$ km) based on their new *Herschel* observations combined with (only) the older *Spitzer* data. The density we derive from the new or old *Spitzer* data places Typhon squarely in the grouping of small, very low density TNOs of Fig. 8. If the Müller et al. diameter is more accurate, then the density would be higher (0.8 g/cm^3), but still below the density of water ice. Thus, the measured densities of small TNO binaries indicate that those objects are probably both compositionally dominated by water ice (expected to be by far the dominant ice on cosmochemical grounds), and also include significant volumes of void space in their interiors (even the upper limits on their density uncertainties lie below 1 g/cm^3). These density, compositional, and structural clues should inform models of collisions and collisional evolution for TNOs.

6.3. Binary formation scenarios

Noll et al. (2008) show that the size ratios (d_2/d_1) for larger TNOs are generally smaller than for smaller TNOs. As noted by Brown et al. (2006), not only are the satellites of the largest TNOs smaller relative to their primaries than for the smaller TNOs, the rate of occurrence of satellites around the large TNOs (3 of 4 objects) is also unusually high. In addition, two of the four systems have multiple satellites. They argue that these unique qualities suggest that the relatively small satellites of large TNOs formed differently than did the relatively large satellites of the smaller TNOs. Their preferred formation scenario for the former was through very large collisions that would have produced disks of debris around the primary, with moonlets coalescing from those disks. They also suggest that such processes could be responsible for the formation of rotationally distorted objects such as Varuna (without known satellites), and Haumea.

Several other studies propose models of binary formation that do not rely on massive, disk-producing impacts. These models fall into two general categories: capture via three (or more) body interactions (Goldreich et al., 2002; Astakhov et al., 2004, 2005; Lee et al., 2007) or collision/capture hybrids (Weidenschilling, 2002; Funato et al., 2004). As discussed by Noll et al. (2008), the capture models tend to produce binary systems that are more consistent with the observed population than do the hybrid models. A weakness of all of these models is that they do not predict that the colors of the binary components should necessarily be similar. For the small binaries with large secondaries, the components have nearly equal colors (*e.g.* Noll et al., 2008; Benecchi et al., 2009). None of these models make specific predictions about the processes that formed the binary components, either, and so do not provide insight into the density we might expect for them.

Nesvorný et al. (2010) propose that the similar colors of binary components are the result of formation by co-accretion from a common concentration of solid material in the protoplanetary disk. If true, this model would also imply very similar bulk compositions for both components of binary TNOs. Their model also tends to produce binaries in which the secondary/primary size ratio is $\gtrsim 0.3$. Most of the known TNO binaries have magnitude differences for the components $\Delta_{mag} < 1$ (implying a size ratio $\gtrsim 0.6$), although that may be due to the difficulty of detecting fainter companions (*e.g.* Noll et al., 2008). For Salacia and (42355) Typhon the secondary/primary size ratios are $\gtrsim 0.3$, consistent with the Nesvorny et al. model. It is interesting that the large ($D > 1000$ km), higher-density objects in Fig. 8 tend to have small satellites (*e.g.* Brown et al., 2006). Pluto-Charon is an obvious exception, but probably formed by an exceptional giant-impact mechanism (*e.g.* Canup, 2011). The smaller, low-density objects tend to have large satellites. In the context of the models mentioned above, it seems possible to draw a tentative conclusion that impacts capable of forming satellite(s) also result in objects with higher densities. Unfortunately, it is extremely difficult to compare the densities of such systems to those of large TNOs lacking satellites (because it is impractical to measure the densities of such objects), or to large TNOs with large captured or co-accreted satellites (because none are known). Thus any causal link between giant-impact and high density remains speculative. If such a link does exist, the density of (120347) Salacia–Actaea may be representative of the bulk compositions and interior structure of large TNOs prior to the kinds of impacts that result in high densities.

6.4. Tidal evolution

Over time, tidal dissipation can circularize mutual orbits and synchronize primary and secondary spins with their orbital periods. The rate of tidal dissipation in a binary system is a sensitive function of the size, separation, and mechanical and material properties of the bodies. For strongly gravity-dominated or fluid bodies, much of the physics of tidal dissipation is captured by the tidal dissipation parameter, Q. $1/Q$ is the fraction of the energy associated with a tidal distortion that is converted via friction into heat, and thus extracted from the orbital motion of the system. We assume $Q = 100$, as is typically done following the analysis presented by Goldreich and Soter (1966).

For solid objects, where material strength is greater than or comparable to gravitational stresses in the interior (as is the case for Typhon, as we discussed earlier), tidal dissipation is somewhat different. In this case, the rigidity of the material leads to a modification of the tidal dissipation parameter (Goldreich and Soter, 1966), given by:

$$Q' = Q\left(1 + \frac{19\mu}{2g\rho R}\right).$$

Here μ is the rigidity (which we assume is between 10^7 dyn cm^{-2} (like that of unconsolidated sand) and 5×10^{10} dyn cm^{-2} (like solid ice) (*e.g.* Yoder, 1982; Gladman et al., 1996)). R is the radius of the object, g is the acceleration of gravity at the object's surface, ρ the mass density (including effects of porosity). We evaluate Q' using R and g for the primary because most of the tidal dissipation occurs there, not in the secondary. All of these considerations lead to values of Q' in the range 100–7000 (Salacia), and 100–2×10^6 (Typhon). Thus tidal dissipation is expected to be more efficient on the gravity-dominated Salacia than it is on Typhon. The large uncertainties in these timescales result from the highly uncertain range of values for μ, coupled with the multiple dependences (g, R and ρ) on the size.

Using the expressions for the timescales to circularize the orbit and to de-spin the primary (Goldreich and Soter, 1966; see also Grundy et al., 2007 and Noll et al., 2008), we estimate the timescales for these processes on Salacia and (42355) Typhon. We assume initial spin periods of 10 h for the primary (*e.g.* Trilling and Bernstein, 2006; Dotto et al., 2008), and account for the uncertainties in the sizes, masses, and densities of the binary components. The timescales for despinning the primaries range from 2×10^6–7×10^9 yr (Salacia), and 1×10^6–4×10^{13} yr (Typhon). As discussed earlier, there is weak evidence for rotation periods of several hours for both objects; if borne out by further evidence of non-synchronous rotation it will be possible to place lower bounds on the Q' values, and thus the rigidity, for both of these objects. The timescales to circularize the binary orbits paint a somewhat clearer picture: for Salacia that timescale is less than 18 Myr, while for Typhon it could be as long as 700 Gyr. Clearly, the Salacia system should have a circular orbit (which it nearly does), while the orbit of Typhon need not be circular.

Typhon's eccentric orbit could be due to recent encounters with Uranus, or other TNOs, in which case considerations of tidal dissipation tell us little about its interior. Updating the estimates made by Noll et al. (2006b) for the actual binary separation of the Typhon system, we find that the encounter distance at which Uranus (or Neptune) could disrupt the binary is 0.024 AU (compared to their estimate of 0.007 AU). Their Fig. 4 then indicates a roughly 5% probability that encounters with Uranus should have disrupted the binary by now, and about a 2% chance that any of Jupiter, Saturn or Neptune would have, for a total disruption probability of roughly 10%. Presumably more distant (and more likely) encounters could excite the eccentricity without disruption. Thus, it seems quite possible that the current eccentricity does not reflect only the effect of tidal dissipation acting to circularize an originally eccentric binary orbit.

However, if we do assume that the current eccentricity of the orbit of Typhon reflects the fact that it formed on an eccentric orbit, rather than being due to some recent perturbation, we can derive a lower bound on Typhon's rigidity by equating the circularization timescale to the age of the Solar System. For our nominal size and mass of the system, we find that the rigidity must be at least $\mu_{min} = 4 \times 10^{10}$ dyn cm^{-2}, very close to that of water ice. This suggests that the interior of Typhon, while significantly porous, is actually quite rigid: it probably is not made up of blocks of material with no cohesion between them. As noted earlier, the high porosity of Typhon also probably requires significant cohesion. If the rigidity of Typhon is indeed this large, then we would expect insignificant amounts of tidal despinning of the components. If the applicable rigidity for Salacia is the same as for Typhon, the rotation rate of the primary of that system may have undergone some degree of tidal evolution, and we would expect a rather long rotation period for it relative to single TNOs or Typhon.

7. Conclusions

Our results show that (120347) Salacia is among the largest of the known TNOs, with component diameters 905 ± 80 and 303 ± 27 km. With a visual geometric albedo less than 4.3%, it is the darkest TNO in the *Spitzer* sample in this size range. The orbital period, 5.49 days, and semi-major axis, 5500 km, give a mass for the system of 4.4×10^{20} kg. Taken together with the diameter, we find that the mass density for the system is $1.1^{+0.41}_{-0.28}$ g/cm^3, lower than any of the other ~1000 km TNOs. If Salacia is made up of both silicates and water ice, the low density requires that it must be significantly porous. We suggest that the density of Salacia (and of Orcus) are indicative of the primordial densities of the larg-

est planetesimals that formed in the outer Solar System, and that densities higher than that result from additional processing (differentiation and/or giant impact). Based on the above findings, we calculate that Salacia should have undergone enough tidal evolution to circularize the binary orbit (consistent with the small observed orbital eccentricity), but that the spin of the primary need not be tidally locked. Based on these and other of the physical properties of Salacia, we conclude that it is unlikely to be a member of the Haumea collisional family.

Our new *Spitzer* observations of (42355) Typhon–Echidna largely confirm our previous results regarding its size and albedo, and recent *Herschel* values for those parameters. Further, all of these results, taken together with the previously published mass for the system, confirm that Typhon is another one of the small ($D \leqslant 500$ km) TNOs with densities well below 1 g/cm^3. Such low densities require these objects to include large fractions of void space in their interiors, particularly if their bulk compositions include any significant amounts of silicates. If the eccentricity of Typhon's binary is not due to recent encounters with the giant planets, considerations of tidal evolution show that the rigidity of the material making up the primary to be about equal to the rigidity expected for water ice. This indicates that Typhon, rather than being a rubble-pile, is a highly competent, yet porous, object.

Acknowledgments

This work is based in part on NASA/ESA *Hubble* Space Telescope observations from Cycle 14 program 10514 and Cycle 16 program 11178. Support for these programs was provided by NASA through grants from the Space Telescope Science Institute (STScI), which is operated by the Association of Universities for Research in Astronomy, Inc., under NASA contract NAS 5–26555. We are especially grateful to Tony Roman at STScI for his quick action in scheduling HST follow-up observations in program 11178. This work is also based in part on *Spitzer Space Telescope* programs 30081 and 40016. *Spitzer* is operated by the Jet Propulsion Laboratory, California Institute of Technology under a contract with NASA through an award issued by JPL/Caltech.

Some of the data presented herein were obtained at the W.M. Keck Observatory, which is operated as a scientific partnership among the California Institute of Technology, the University of California and the National Aeronautics and Space Administration. The Observatory was made possible by the generous financial support of the W.M. Keck Foundation. The authors wish to recognize and acknowledge the very significant cultural role and reverence that the summit of Mauna Kea has always had within the indigenous Hawaiian community. We are most fortunate to have the opportunity to conduct observations from this mountain.

W.M.G., S.B.P., and H.G.R. gratefully acknowledge partial support from NSF Planetary Astronomy Grant AST-1109872.

References

Altenhoff, W.J., Bertoldi, F., Menten, K.M., 2004. Size estimates of some optically bright KBOs. Astron. Astrophys. 415, 771–775.

Astakhov, S.A., Farrelly, D., 2004. Capture and escape in the elliptic restricted three-body problem. Monthly Notices Roy. Astron. Soc 354, 971–979.

Astakhov, S.A., Lee, E.A., Farrelly, D., 2005. Formation of Kuiper-belt binaries through multiple chaotic scattering encounters with low-mass intruders. Monthly Notices Roy. Astron. Soc. 360, 401–415.

Barucci, M.A., Brown, M.E., Emery, J.P., Merlin, F., 2008a. Composition and surface properties of transneptunian objects and centaurs. In: Barucci, M.A., Boehnhardt, H., Cruikshank, D.P., Morbidelli, A. (Eds.), The Solar System Beyond Neptune. Univ. of Arizona Press, Tucson, AZ, pp. 143–160.

Barucci, M.A. et al., 2008b. Surface composition and temperature of the TNO Orcus. Astron. Astrophys. 479, L13–L16.

Benecchi, S.D., Noll, K.S., Grundy, W.M., Buie, M.W., Stephens, D., Levison, H.F., 2009. The correlated colors of transneptunian binaries. Icarus 200, 292–303.

Benecchi, S.D., Noll, K.S., Grundy, W.M., Levison, H.F., 2010. (47171) 1999 TC_{36}. A transneptunian triple. Icarus 207, 978–991.

Bowell, E., Hapke, B., Domingue, D., Lumme, K., Peltoniemi, J., Harris, A.W., 1989. Application of photometric models to asteroids. In: Binzel, R.P., Gehrels, T., Matthews, M.S. (Eds.), Asteroids II. Univ. of Arizona Press, Tucson, AZ, pp. 524–556.

Braga-Ribas, F. et al., 2011. Stellar occultations by TNOs: The January 08, 2011 by (208996) 2003 AZ84 and the May 04, 2011 by (50000) Quaoar. In: EPSC-DPS Joint Meeting 2011 1060.

Brown, M.E. et al., 2006. Satellites of the Largest Kuiper Belt Objects. Astrophys. J 639, L43–L46.

Brown, M.E., Schaller, E.L., 2007. The mass of dwarf planet eris. Science 316, 1585.

Brown, M.E., Barkume, K.M., Ragozzine, D., Schaller, E.L., 2007. A collisional family of icy objects in the Kuiper belt. Nature 446, 294–296.

Brown, M.E., Ragozzine, D., Stansberry, J., Fraser, W.C., 2010. The size, density, and formation of the Orcus–Vanth system in the Kuiper belt. Astron. J. 139, 2700–2705.

Brucker, M.J., Grundy, W.M., Stansberry, J.A., Spencer, J.R., Sheppard, S.S., Chiang, E.I., Buie, M.W., 2009. High albedos of low inclination classical Kuiper belt objects. Icarus 201, 284–294.

Canup, R.M., 2011. On a giant impact origin of Charon, Nix, and Hydra. Astron. J. 141, 35–43.

Cruikshank, D.P. et al., 2005. The high-Albedo Kuiper belt object (55565) 2002 AW_{197}. Astrophys. J. 624, L53–L56.

Delbó, M., Harris, A.W., Binzel, R.P., Pravec, P., Davies, J.K., 2003. Keck observations of near-Earth asteroids in the thermal infrared. Icarus 166, 116–130.

DeMeo, F.E. et al., 2009. Visible and near-infrared colors of transneptunian objects and Centaurs from the second ESO large program. Astron. Astrophys. 493, 283–290.

Doressoundiram, A., Boehnhardt, H., Tegler, S.C., Trujillo, C., 2008. Color properties and trends of the transneptunian objects. In: Barucci, M.A., Boehnhardt, H., Cruikshank, D.P., Morbidelli, A. (Eds.), The Solar System Beyond Neptune. Univ. of Arizona Press, Tucson, AZ, pp. 91–104.

Dotto, E. et al., 2008. Rotational properties of Centaurs and trans-neptunian objects. Lightcurves and densities. Astron. Astrophys. 490, 829–833.

Elliot, J.L. et al., 2005. The deep ecliptic survey: A search for Kuiper belt objects and Centaurs. II. Dynamical classification, the Kuiper belt plane, and the core population. Astron. J. 129, 1117–1162.

Elliot, J.L. et al., 2010. Size and albedo of Kuiper belt object 55636 from a stellar occultation. Nature 465, 897–900.

Engelbracht, C.W. et al., 2007. Absolute Calibration and Characterization of the Multiband Imaging Photometer for Spitzer. I. The Stellar Calibrator Sample and the 24 μm Calibration, vol. 119. Astronomical Society of the Pacific, pp. 994–1018.

Fernández, Y.R., Sheppard, S.S., Jewitt, D.C., 2003. The albedo distribution of jovian trojan asteroids. Astron. J. 126, 1563–1574.

Ford, H.C., the ACS Science Team, 1996. The advanced camera for the Hubble Space Telescope. In: Bely, P., Breckinridge, J. (Eds.), Space Telescopes and Instruments IV, Proc. SPIE 2807. Cambridge Univ. Press, Cambridge, pp. 184–196.

Fraser, W.C., Brown, M.E., 2010. Quaoar: A rock in the Kuiper belt. Astrophys. J. 714, 1547–1550.

Funato, Y., Makino, J., Hut, P., Kokubo, E., Kinoshita, D., 2004. The formation of Kuiper-belt binaries through exchange reactions. Nature 427, 518–520.

Gladman, B., Dane Quinn, D., Nicholson, P., Rand, R., 1996. Synchronous locking of tidally evolving satellites. Icarus 122, 166–192.

Gladman, B., Marsden, B.G., Vanlaerhoven, C., 2008. Nomenclature in the Outer Solar System. In: Barucci, M.A., Boehnhardt, H., Cruikshank, D.P., Morbidelli, A. (Eds.), The Solar System Beyond Neptune. Univ. of Arizona Press, Tucson, AZ, pp. 43–57.

Goldreich, P., Soter, S., 1966. Q in the Solar System. Icarus 5, 375–389.

Goldreich, P., Lithwick, Y., Sari, R., 2002. Formation of Kuiper-belt binaries by dynamical friction and three-body encounters. Nature 420, 643–646.

Gomes, R., 2003. The common origin of the high inclination TNO's. Earth, Moon Planets 92, 29–42.

Gomes, R.S., 2011. The origin of TNO 2004 XR_{190} as a primordial scattered object. Icarus 215, 661–668.

Gordon, K.D. et al., 2005. Reduction Algorithms for the Multiband Imaging Photometer for Spitzer, vol. 117. Astronomical Society of the Pacific, pp. 503–525.

Gordon, K.D. et al., 2007. Absolute Calibration and Characterization of the Multiband Imaging Photometer for Spitzer. II. 70 μm Imaging, vol. 119. Astronomical Society of the Pacific, pp. 1019–1037.

Grundy, W.M., Stansberry, J.A., Noll, K.S., Stephens, D.C., Trilling, D.E., Kern, S.D., Spencer, J.R., Cruikshank, D.P., Levison, H.F., 2007. The orbit, mass, size, albedo, and density of (65489) Ceto/Phorcys: A tidally-evolved binary Centaur. Icarus 191, 286–297.

Grundy, W.M., Noll, K.S., Virtanen, J., Muinonen, K., Kern, S.D., Stephens, D.C., Stansberry, J.A., Levison, H.F., Spencer, J.R., 2008. (42355) Typhon Echidna: Scheduling observations for binary orbit determination. Icarus 197, 260–268.

Grundy, W.M., Noll, K.S., Buie, M.W., Benecchi, S.D., Stephens, D.C., Levison, H.F., 2009. Mutual orbits and masses of six transneptunian binaries. Icarus 200, 627–635.

Grundy, W.M., Noll, K.S., Nimmo, F., Roe, H.G., Buie, M.W., Porter, S.B., Benecchi, S.D., Stephens, D.C., Levison, H.F., Stansberry, J.A., 2011. Five new and three improved mutual orbits of transneptunian binaries. Icarus 213, 678–692.

Harris, A.W., 1998. A thermal model for near-Earth asteroids. Icarus 131, 291–301.

Jewitt, D.C., Sheppard, S.S., 2002. Physical properties of trans-neptunian object (20000) Varuna. Astron. J. 123, 2110–2120.

Jewitt, D., Aussel, H., Evans, A., 2001. The size and albedo of the Kuiper-belt object (20000) Varuna. Nature 411, 446–447.

Kiss, C. et al., 2011. Sedna, Eris and Quaoar: Physical properties of prominent trans-neptunian objects, based on Herschel observations. In: EPSC-DPS Joint Meeting 2011 1124.
Krist, J.E., Hook, R.N., 2004. The Tiny Tim User's Guide. Version 6.3. Space Telescope Science Institute, Baltimore, <http://www.stsci.edu/software/tinytim>.
Lebofsky, L.A., Sykes, M.V., Tedesco, E.F., Veeder, G.J., Matson, D.L., Brown, R.H., Gradie, J.C., Feierberg, M.A., Rudy, R.J., 1986. A refined 'standard' thermal model for asteroids based on observations of 1 Ceres and 2 Pallas. Icarus 68, 239–251.
Lee, E.A., Astakhov, S.A., Farrelly, D., 2007. Production of trans-neptunian binaries through chaos-assisted capture. Monthly Notices Roy. Astron. Soc. 379, 229–246.
Lellouch, E. et al., 2010. "TNOs are cool": A survey of the trans-neptunian region. II. The thermal lightcurve of (136108) Haumea. Astron. Astrophys. 518, L147.
Lellouch, E., Stansberry, J., Emery, J., Grundy, W., Cruikshank, D.P., 2011. Thermal properties of Pluto's and Charon's surfaces from Spitzer observations. Icarus 214, 701–716.
Le Mignant, D. et al. 2006. LGS AO at W.M. Keck Observatory: Routine operations and remaining challenges. Proc. SPIE 6272, 627201.
Lim, T.L. et al., 2010. "TNOs are Cool": A survey of the trans-neptunian region. III. Thermophysical properties of 90482 Orcus and 136472 Makemake. Astron. Astrophys. 518, L148.
Maris, M., Carraro, G., 2008. An analysis of the Eris (2003 UB_{313}) light curve. Planetary and Space Science 56, 1874–1877.
McKinnon, W.B., Durham, W.B., Stern, L.A., 2005. Cold compaction of porous ice, and the densities of Kuiper belt objects. Paper presented at: Asteroids, Comets, and Meteors, Rio de Janeiro, Brazil, August 7-12, 2005.
McKinnon, W.B., Simonelli, D.P., Schubert, G., 1997. Composition, Internal Structure, and Thermal Evolution of Pluto and Charon. Pluto and Charon 295.
McMaster, M. et al., 2008. WFPC2 Instrument Handbook. Version 10.0. Space Telescope Science Institute, Baltimore, <http://www.stsci.edu/hst/wfpc2>.
Müller, T.G. et al., 1999. Fundamental Thermal Emission Parameters of Main-Belt Asteroids Derived from ISO. The Universe as Seen by ISO 427, p. 141.
Müller, T.G. et al., 2010. "TNOs are Cool": A survey of the trans-neptunian region. I. Results from the Herschel science demonstration phase (SDP). Astron. Astrophys. 518, L146.
Nesvorný, D., Youdin, A.N., Richardson, D.C., 2010. Formation of Kuiper belt binaries by gravitational collapse. Astron. J. 140, 785–793.
Noll, K.S., Levison, H.F., Stephens, D.C., Grundy, W.M., 2006a. (120347) 2004 SB_60. International Astronomical Union Circular 8751, p. 1.
Noll, K.S., Grundy, W.M., Stephens, D.C., Levison, H.F., 2006b. (42355) 2002 CR_46. International Astronomical Union Circular 8689, p. 1.
Noll, K.S., Grundy, W.M., Chiang, E.I., Margot, J.-L., Kern, S.D., 2008. Binaries in the Kuiper belt. In: Barucci, M.A., Boehnhardt, H., Cruikshank, D.P., Morbidelli, A. (Eds.), The Solar System Beyond Neptune. Univ. of Arizona Press, Tucson, AZ, pp. 345–363.
Ortiz, J.L., Gutiérrez, P.J., Casanova, V., Sota, A., 2003. A study of short term rotational variability in TNOs and Centaurs from Sierra Nevada Observatory. Astron. Astrophys. 407, 1149–1155.
Parker, A.H., Kavelaars, J.J., 2012. Collisional evolution of ultra-wide trans-neptunian binaries. Astrophys. J. 744, 139–152.
Parker, A.H., Kavelaars, J.J., Petit, J.-M., Jones, L., Gladman, B., Parker, J., 2011. Characterization of seven ultra-wide trans-neptunian binaries. Astrophys. J. 743, 1–20.
Rabinowitz, D.L. et al., 2006. Photometric observations constraining the size, shape, and Albedo of 2003 EL61, a rapidly rotating, Pluto-sized object in the Kuiper belt. Astrophys. J. 639, 1238–1251.
Rabinowitz, D.L., Schaefer, B.E., Tourtellotte, S.W., 2007. The diverse solar phase curves of distant icy bodies. I. Photometric observations of 18 trans-neptunian objects, 7 Centaurs, and Nereid. Astron. J. 133, 26–43.
Ragozzine, D., Brown, M.E., 2007. Candidate Members and Age Estimate of the Family of Kuiper Belt Object 2003 EL61. Astron. J 134, 2160–2167.
Ragozzine, D., Brown, M.E., 2009. Orbits and masses of the satellites of the dwarf planet Haumea (2003 EL61). Astron. J. 137, 4766–4776.
Rieke, G.H. et al., 2004. The multiband imaging photometer for Spitzer (MIPS). Astrophys. J. 154 (Suppl.), 25–29.
Rieke, G.H. et al., 2008. Absolute physical calibration in the infrared. Astron. J. 135, 2245–2263.
Russel, H.N., 1916. On the albedo of the planets and their satallites. Astrophys. J. 43, 173–196.
Roe, H.G., Brown, M.E., Barkume, K.M., Marsden, B.G., 2005. Seven TNOs. Minor Planet Electronic Circulars 26.
Santos-Sanz, P. et al., 2012. "TNOs are Cool": A survey of the trans-neptunian region. IV. Size/albedo characterization of 15 scattered disk and detached objects observed with Herschel/PACS. Astron. Astrophys., forthcoming.
Schaller, E.L., Brown, M.E., 2008. Detection of additional members of the 2003 EL61 collisional family via near-infrared spectroscopy. Astrophys. J. 684, L107–L109.
Sheppard, S.S., 2007. Light curves of dwarf plutonian planets and other large Kuiper belt objects: Their rotations, phase functions, and absolute magnitudes. Astron. J. 134, 787–798.
Sheppard, S.S., Lacerda, P., Ortiz, J.L., 2008. Photometric lightcurves of transneptunian objects and centaurs: Rotations, shapes, and densities. In: Barucci, M.A., Boehnhardt, H., Cruikshank, D.P., Morbidelli, A. (Eds.), The Solar System Beyond Neptune. Univ. of Arizona Press, Tucson, AZ, pp. 129–142.
Sheppard, S.S., Ragozzine, D., Trujillo, C., 2012. 2007 TY430: A cold classical Kuiper belt type binary in the plutino population. Astron. J. 143, 58–70.
Sicardy, B. et al., 2011. A Pluto-like radius and a high albedo for the dwarf planet Eris from an occultation. Nature 478, 493–496.
Snodgrass, C., Carry, B., Dumas, C., Hainaut, O., 2010. Characterisation of candidate members of (136108) Haumea's family. Astron. Astrophys. 511, A72.
Spencer, J.R., 1990. A rough-surface thermophysical model for airless planets. Icarus 83, 27–38.
Spencer, J.R., Lebofsky, L.A., Sykes, M.V., 1989. Systematic biases in radiometric diameter determinations. Icarus 78, 337–354.
Spencer, J.R., Stansberry, J.A., Grundy, W.M., Noll, K.S., 2006. A low density for binary Kuiper belt object (26308) 1998 SM165. Bull. Am. Astron. Soc. 38, 546.
Stansberry, J.A. et al., 2006. The Albedo, size, and density of binary Kuiper belt object (47171) 1999 TC_{36}. Astrophys. J. 643, 556–566.
Stansberry, J.A. et al., 2007. Absolute Calibration and Characterization of the Multiband Imaging Photometer for Spitzer. III. An Asteroid-based Calibration of MIPS at 160 μm, vol. 119. Astronomical Society of the Pacific, pp. 1038–1051.
Stansberry, J., Grundy, W., Brown, M., Cruikshank, D., Spencer, J., Trilling, D., Margot, J.-L., 2008. Physical properties of Kuiper belt and centaur objects: Constraints from the Spitzer space telescope. in: Barucci, M.A., Boehnhardt, H., Cruikshank, D.P., Morbidelli, A. (Eds.), The Solar System Beyond Neptune. Univ. of Arizona Press, Tucson, AZ, pp. 161–179.
Tegler, S.C., Romanishin, W., Consolmagno, G.J., 2003. Color patterns in the Kuiper belt: A possible primordial origin. Astrophys. J. 599, L49–L52.
Thirouin, A., Ortiz, J.L., Duffard, R., Santos-Sanz, P., Aceituno, F.J., Morales, N., 2010. Short-term variability of a sample of 29 trans-neptunian objects and Centaurs. Astron. Astrophys. 522, A93.
Trilling, D.E., Bernstein, G.M., 2006. Light curves of 20–100 km Kuiper belt objects using the hubble space telescope. Astron. J. 131, 1149–1162.
Trujillo, C.A., Sheppard, S.S., Schaller, E.L., 2011. A photometric system for detection of water and methane ices on Kuiper belt objects. Astrophys. J 730, 105.
Vilenius, E. et al., 2012. "TNOs are Cool": A survey of the trans-neptunian region. VI. Herschel/PACS observations and thermal modeling of 19 classical Kuiper belt objects. Astron. Astrophys., forthcoming.
Weidenschilling, S.J., 2002. On the origin of binary transneptunian objects. Icarus 160, 212–215.
Yoder, C.F., 1982. Tidal rigidity of PHOBOS. Icarus 49, 327–346.